Astronomy & Astrophysics manuscript no. arxiv_version
January 6, 2023

Temperature of Solar Orbiter/EUI quiet Sun small scale brightenings: evidence for a cooler component

A. Dolliou[1], S. Parenti[1], F. Auchère[1], K. Bocchialini[1], G. Pelouze[1], P. Antolin[2], D. Berghmans[3], L. Harra[4,5], D. M. Long[6], U. Schühle[7], E. Kraaikamp[3], K. Stegen[3], C. Verbeeck[3], S. Gissot[3], R. Aznar Cuadrado[7], E. Buchlin[1], M. Mierla[3,8], L. Teriaca[7], and A. N. Zhukov[3,9]

[1] Université Paris-Saclay, CNRS, Institut d'astrophysique spatiale, 91405, Orsay, France
[2] Department of Mathematics, Physics and Electrical Engineering, Northumbria University, Newcastle Upon Tyne, NE1 8ST, UK
[3] Solar-Terrestrial Centre of Excellence – SIDC, Royal Observatory of Belgium, Ringlaan -3- Av. Circulaire, 1180 Brussels, Belgium
[4] Physikalisch-Meteorologisches Observatorium Davos, World Radiation Center, 7260, Davos Dorf, Switzerland
[5] ETH-Zürich, Wolfgang-Pauli-Str. 27, 8093 Zürich, Switzerland
[6] UCL-Mullard Space Science Laboratory, Holmbury St. Mary, Dorking, Surrey, RH5 6NT, UK
[7] Max Planck Institute for Solar System Research, Justus-von-Liebig-Weg 3, 37077 Göttingen, Germany
[8] Institute of Geodynamics of the Romanian Academy, Bucharest, Romania
[9] Skobeltsyn Institute of Nuclear Physics, Moscow State University, 119992 Moscow, Russia
e-mail: antoine.dolliou@universite-paris-saclay.fr

Received 7 September 2022 / Accepted 4 January 2023

ABSTRACT

Context. On 2020 May 30, small and short-lived EUV brightenings were observed in the Quiet Sun (QS) during a four minutes sequence by EUI/HRI$_{EUV}$ on board Solar Orbiter. Their physical origin and possible impact on coronal or Transition Region (TR) heating are still to be determined.
Aims. Our aim is to derive the statistical thermal evolution of these events in order to establish their coronal or TR origin.
Methods. Our thermal analysis takes advantage of the multithermal sensitivity of the Atmospheric Imaging Assembly (AIA) imager on board the Solar Dynamics Observatory (SDO). We first identified these HRI$_{EUV}$ events in the six coronal bands of AIA. We then performed a statistical time lag analysis, which quantifies the delays between the light curves from different bands. These time lags can give significant insights into the temperature evolution of these events. The analysis is performed taking into account the possible contribution to the results from the background and foreground emissions.
Results. The events are characterized by time lags inferior to the AIA cadence of 12 s, for all nine couples of AIA bands analyzed. Our interpretation is the possible co-presence of events which reach or do not reach coronal temperatures (≈ 1 MK). We believe that the cool population dominates the events analyzed in this work.

Key words. Sun: corona – Sun: transition region – Sun: UV radiation – Instrumentation: high angular resolution

1. Introduction

Decades of investigation suggest that the solar corona is formed and maintained through small scale processes, even though the mechanisms at the origin of such processes are only partially understood. Waves dissipation and magnetic field reconnection are present in the solar atmosphere and are the main candidates processes for the plasma heating. See for instance Reale (2014) and Viall et al. (2021) for a review on the argument.

The observations suggest that the dissipation of magnetic energy leading to coronal heating must happen at unresolved spatial scales, and while many dissipation mechanisms are impulsive in nature, it is unclear whether the dissipation has a more continuous or bursty character on average. The properties of these heating events, such as their amplitude, the duration and the occurrence frequency, are still a matter of debate.

Parker (1988) proposed magnetic reconnection as the origin of these heating events (which became known as nanoflares). His theory is based on the shuffling and intermixing of the photospheric footpoints of magnetic flux tubes, which would produce reconnection with subsequent formation of tiny current sheets in which the energy is dissipated. This idea has been generalized in more recent years, particularly for active region heating, where other processes (waves propagation) than reconnection may also be at the origin of the nanoflares energy (Van Doorsselaere et al. 2020; Viall et al. 2021). For instance, small scale energy dissipation can occur through turbulent cascade created by nonlinear waves interaction (e.g. Buchlin & Velli 2007), or through shock heating from nonlinear mode conversion (Moriyasu et al. 2004).

Studies addressing the heating of the Quiet Sun (QS) indicate that waves and reconnections are also present (e.g. McIntosh et al. 2011; Hahn & Savin 2014; Upendran & Tripathi 2021, 2022). Observations of the corona from the hard X-rays (e.g. Crosby et al. 1993; Shimizu 1995; Hannah et al. 2010) to the UV bands (e.g. Berghmans et al. 1998; Harra et al. 2000; Aschwanden & Parnell 2002) also suggest that small scale impulsive heating may play a role here. These observations reveal that unresolved small bright transient events increase in number everywhere in the corona, any time we increase the spatial and temporal resolutions of our instruments.

Examples of small and fast phenomena in the corona have been observed during the High-Resolution Coronal Imager (Hi-

C) sounding rocket flights (Kobayashi et al. 2014), during which images were recorded in a band centered on 193 Å (including the Fe XII 195 Å line). These observations were made with a spatial resolution of about 0.3″ (≈ 220 km, Winebarger et al. 2014). The Hi-C instrument resolved small cool loops (Winebarger et al. 2013) and EUV bright dots with characteristic lengths of 680 km, durations of 25 s and temperatures ranging between 0.5 and 1.5 MK (Régnier et al. 2014).

The Interface Region Imaging Spectrograph (IRIS; De Pontieu et al. 2014) reaches a resolution of ≈ 0.33″ – 0.4″ (≈ 240 – 290 km in the corona), but is mostly sensitive to transition region (TR) and chromospheric temperatures. With IRIS and SDO/AIA (Solar Dynamics Observatory, Pesnell et al. 2012) it was possible, for instance, to observe tiny, short-lived and multithermal "nanojets" (size 1000 – 2000 km, ∼15 s, with chromospheric to coronal temperatures, Antolin et al. 2021; Sukarmadji et al. 2022) in large cool loops, interpreted as the transverse motion of field lines reconnecting at small angles. Larger jet-like structures (Innes & Teriaca 2013) were detected with the Solar Ultraviolet Measurements of Emitted Radiation (SUMER) spectrometer (Wilhelm et al. 1995) on board the Solar and Heliospheric Observatory (SOHO), along with Ultraviolet (UV) (Peter et al. 2014) and Extreme-UV (EUV) (Young et al. 2018) bursts. IRIS has also observed 'unresolved fine structures' (UFS) in TR lines, which has been associated with short (≈ 4 – 12 Mm) loops or part of loops. They were seen at the limb in QS regions, and showed to be highly variable (few minutes), with strong Doppler shift dynamics (up to 100 km s^{-1}).

Besides the aforementioned sporadic and short duration Hi-C rocket flights, the Atmospheric Imaging Assembly (AIA, Lemen et al. 2012), onboard the Solar Dynamics Observatory (SDO, Pesnell et al. 2012) obtains full Sun images with a resolution of 1.5″, corresponding to ≈ 1100 km in the corona). Using the AIA 171 and 193 Å channels, Raouafi & Stenborg (2014) detected small jets ("jetlets") at the footpoint of coronal plumes. More recently, Chitta et al. (2021) characterised the statistical properties of small EUV bursts detected in AIA 171, 193 and 211 Å sequences.

The Solar Orbiter mission (Müller, D. et al. 2020; Zouganelis et al. 2020) carries, as part of the remote-sensing payload (Auchère et al. 2020), the Extreme Ultraviolet Imager (EUI) suite (Rochus et al. 2020). The High-Resolution Imager (HRI_{EUV}) and the Full Sun Imager (FSI) 174 channels are dominated by emission from lines of Fe IX and Fe X. They image the plasma emission of the high TR and corona, which is the region of interest for this work.

At the closest, Solar Orbiter approaches the Sun down to 0.28 AU, allowing a two pixels spatial resolution of ≈ 200 km on the corona, along with a maximal cadence of 1.6 s, thus providing the highest spatial and temporal resolution images to date at these wavelengths, for extended periods of time and on a variety of targets.

On May 30, 2020, when Solar Orbiter was at 0.556 AU, HRI_{EUV} made its first observation of the QS corona at high resolution (400 km) and cadence (5 s). During this 4 minutes sequence, 1467 small EUV brightenings of variable size (400 to 4000 km) and lifetime (10 to 200 s) have been detected and called "campfires" (Berghmans et al. 2021). The HRI_{EUV} field of view was also visible by SDO/AIA and part of the events detected by HRI_{EUV} were also visible in at least one of the AIA coronal bands, because of the lower spatial and temporal resolutions of AIA (about 1100 km and 12 s, respectively). Berghmans et al. (2021) used the AIA observations to infer their temperature applying the Differential Emission Measure (DEM) diagnostic method of Hannah & Kontar (2012). The resulting distribution was centered around 1.3 MK.

These features have yet to be better characterized, but the first investigations suggest that their origin is linked to photospheric magnetic cancellation (Panesar et al. 2021) or magnetic reconnection close to the TR or the chromospheric part of the loops (Kahil et al. 2022). Zhukov et al. (2021) found that these EUV brightenings are low-lying (1 Mm to 5 Mm), which indicates that they could be chromospheric or transition region features. The authors noticed that the estimated heights of the features are larger than their apparent lengths. If these events are loops, this implies that HRI_{EUV} does not see their full extent. Therefore, if they reach 1 MK, they do so only at their apex.

Winebarger et al. (2013) used Hi-C and SDO/AIA data to estimate the temperature of small inter-moss loops to be about 2.8×10^5 K. These had a projected length between about 5 and 7 Mm and their light curves, from the different AIA bands, peaked at the same time, suggesting the absence of cooling from coronal temperature. These loops are larger than the ones observed by Berghmans et al. (2021) and Zhukov et al. (2021), furthermore they are observed in active regions. However, it is possible that they share similar physical mechanisms.

These results motivated our work to further investigate the thermal properties of the HRI_{EUV} events. We perform a statistical study over more than the 1000 detected events, and the rest of the QS used as a reference (see Sect. 2). Our analysis is based on the time lag method (see Sect. 3) applied to the AIA light curves from several pairs of channels. This method has been extensively used in active regions to study loops submitted to Thermal Non Equilibrium (TNE; Froment et al. 2015; Froment et al. 2017, 2020; Froment 2016), and to test the nanoflares theory (Viall & Klimchuk 2011; Viall & Klimchuk 2012; Viall & Klimchuk 2015, 2017). The novelty of the present work relies on the application of this technique to QS region data and over short time lags. In Sect. 4, we show that there is no or little sign of lag between all the chosen AIA bands. The implications of these results will be discussed in Sect. 5.

2. Observations and data reduction

On 2020 May 30, while the Solar Orbiter mission was still performing commissioning activities, HRI_{EUV} observed a QS region at 5 seconds cadence for 4 minutes, from 14:54:00 UT to 14:58:05 UT. The field of view of HRI_{EUV} (blue square) is visible in a full Sun image taken in the FSI 174 channel (Fig. 1 (a)). Fig. 1 (c) shows the corresponding field of view on a full Sun image of AIA 171, as seen by SDO, which has a similar temperature response, peaking at 0.9 Mm.

The different apparent position of the HRI_{EUV} field of view between Fig. 1 (a) and (c) is caused by the separation angle, equal to 31.5° between the Solar Orbiter line of sight and the Sun-Earth line.

2.1. Detection of the EUV brightenings by HRIEUV

The HRI_{EUV} data used for the present work[1] was taken at 0.556 AU from the Sun, resulting in a spatial resolution of ∼ 400 km in the corona. In this sequence, Berghmans et al. (2021) automatically detected and cataloged 1467 brightening events, nicknamed *campfires*, and called *events* from now on. The detection was performed after remapping the images on a

[1] EUI Data Release 1.0 https://doi.org/10.24414/wvj6-nm32

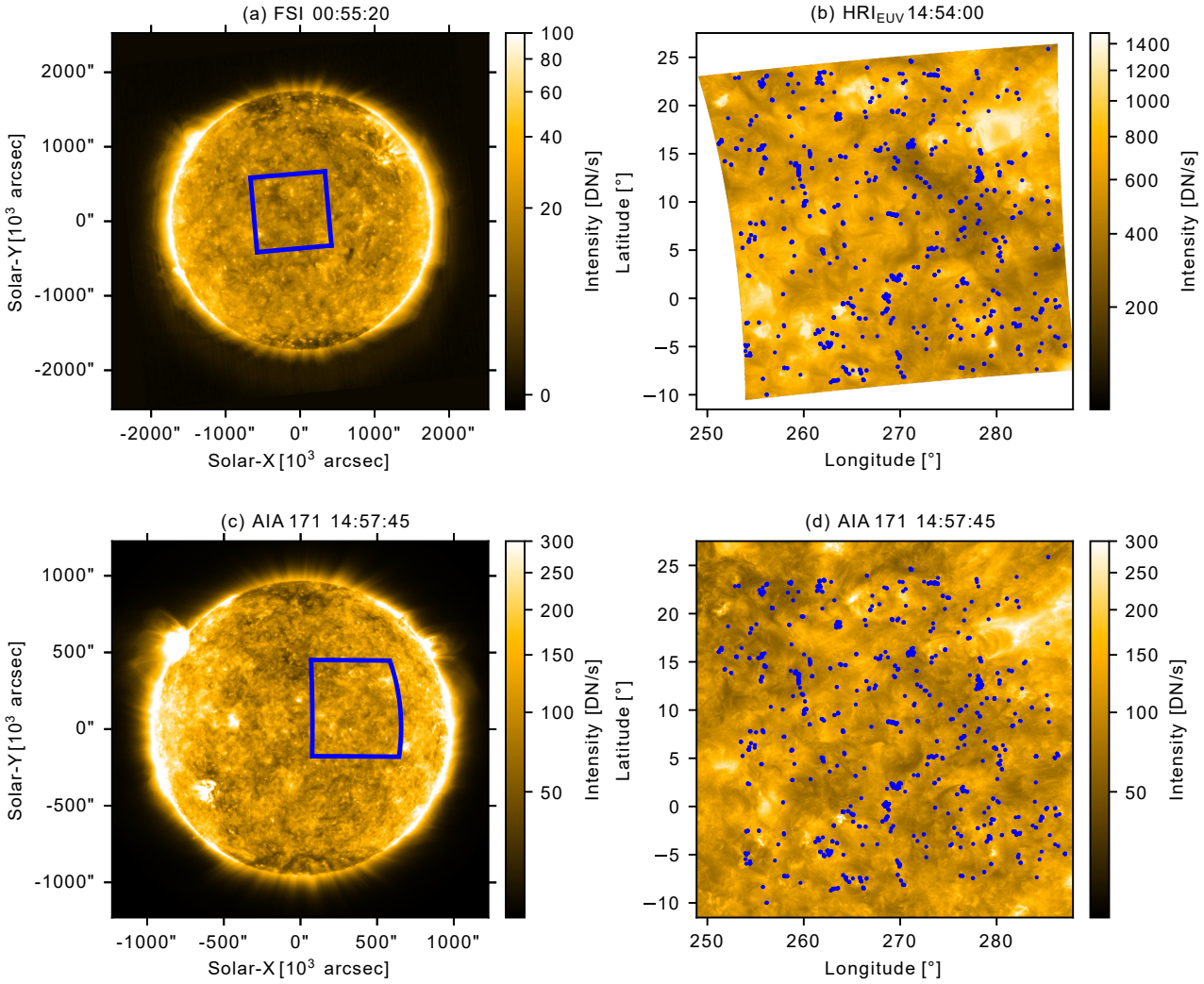

Fig. 1. Images captured on May 30, 2020. *Upper row :* field of view observed by FSI 174 (a), and the first image of the HRI_{EUV} sequence (b) in Carrington coordinates. The FSI image is the closest available to the HRI_{EUV} sequence. *Lower row :* AIA 171 image (c) and remapped on the same grid as HRI_{EUV} (d). Blue rectangles in the left column correspond to the field of view on the right column, and the blue dots in the right column are the positions of the 1467 detected events.

regular 2400 × 2400 Carrington grid spanning from 248.9° to 287.9° in longitude and −11.5° to 27.5° in latitude (corresponding to a 0.016 25° pitch, 198 km on the sphere) with a projection radius of 1.004 $R_\odot$ (Fig. 1). The spacecraft jitter being documented in the FITS headers, it is compensated by the Carrington remapping, and the absolute pointing values were determined by cross-correlation with AIA.

The automated detection scheme (appendix B of Berghmans et al. 2021) defines the events as the pixels whose intensity is larger than an arbitrarily defined threshold of 5 times the local noise level, in the first two smaller scales of a spatial *à trous* wavelet transform. Events overlapping between successive frames were merged to produce the final set of spatio-temporal events. Their surfaces range from 0.04 Mm^2 (the HRI_{EUV} spatial resolution) to 5 Mm^2, the upper limit being partly a consequence of the chosen maximum wavelet scale. No restriction was imposed on their duration. We note that the number of detected events, as well as their properties (surface, lifetime), highly depends upon the detection parameters. For consistency, we used the (Berghmans et al. 2021) cataloged as is. We however removed the events present in the first or last image of the HRI_{EUV} observation, as their lifetime might not have been fully captured. Fig. 1 (b) shows the location of the 1314 selected events on the first HRI_{EUV} image of the sequence.

2.2. Multichannel observations with AIA

A major limitation of HRI_{EUV} is its single passband, which makes it impossible to derive information on the plasma temperature. For this purpose, we used data from 6 channels (94, 131, 171, 193, 211, and 335 Å) of the AIA instrument. We did not include the 304 band because the He II 30.4 nm spectral line is op-

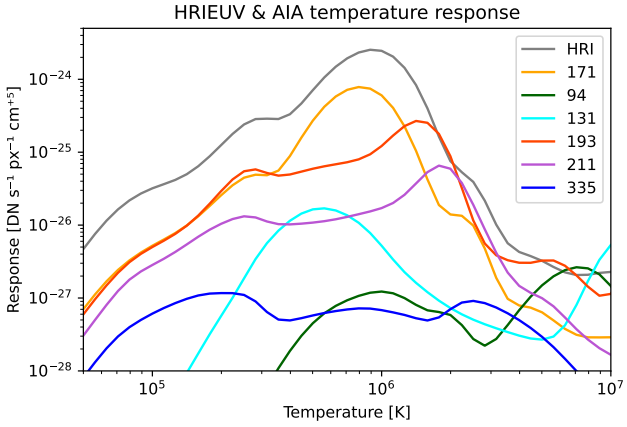

Fig. 2. HRI_{EUV} and AIA temperature response functions computed with CHIANTI 10.0.1 (Dere et al. 1997; Del Zanna et al. 2021), assuming an electron number density $n_e = 10^9$ cm^{-3}.

tically thick and the interpretation of its intensity is not straightforward. The selected bands cover a wide range of plasma temperatures (0.2 MK to 8 MK, Fig. 2), but have only less than half the temporal resolution (12 s) of HRI_{EUV} (5 s).

For our work, we need to take into account the lower spatial and temporal resolutions of AIA, compared with HRI_{EUV}. Therefore, small and short-lived events detected by HRI_{EUV} can be unresolved when observed with AIA 171. In addition, events might not be sufficiently bright in some of the AIA bands to be detectable. The HRI_{EUV} and AIA images have been paired taking into account the 229 s difference in light travel time to Solar Orbiter and to the Earth. The AIA images have been remapped onto the same Carrington grid as the HRI_{EUV} data (Fig. 1, d). On this common grid, the HRI_{EUV} images are re-sampled with at least 1 grid point per pixel, and the AIA images with at least 2.

3. Method

In order to characterize the evolution of the thermal structure of these events, we used the time lags method. Because the AIA bands peak at different temperatures (Fig. 2), time lags between them are a signature of plasma cooling (or heating) over time. For example, the response functions of the AIA 193 and 171 bands peak respectively at 1.5 MK and 0.9 MK. The intensity in the 171 band peaking after the 193 one can be interpreted as a hot plasma cooling. The opposite behavior, can be a signature of plasma heating. We discuss the various possible scenarios in detail in Sect. 5.

We describe below the computation and classification of the AIA light curves (Sect. 3.1), and the computation of the time lags (Sect. 3.2). The analysis is performed pixel-by-pixel to take into account the spatial and the temporal information contained in the data. Several events are spatially resolved in the AIA data, so that the thermal behavior in individual pixels of each event will be independently characterized. This avoids the assumption that the event has no thermal sub-structure. This method may involve the use of low SNR for some of the pixels. This could be avoided by performing the analysis over the integrated intensity from the whole spatial extension of the event. However, the latter choice would impose the above-mentioned assumption, which we prefer to avoid. We verified in Appendix B that a same time lag analysis, performed over whole events, yields the same results.

In the following, we call "background" the total of background and foreground emission superimposed on the events along the line of sight. Background emission can represent a large fraction of the total emission (Sect. 4.3) and has the same properties as the QS emission observed outside events. Since we want to measure the time lags of the events themselves, it is necessary to check the influence of the background (as described in Section 3.1). The background intensity is estimated for each pixel and time step.

3.1. Light curves

For our analysis, we classify the pixels in two categories: the "event" pixels, that is those containing at least one event from Berghmans et al. (2021) during the sequence, and the "non-event" pixels, which we call Quiet Sun (QS) for simplicity. The QS pixels are used as a reference, and their statistics will be compared to that of the event pixels (Sect. 4.3).

While the AIA and HRI_{EUV} data have been re-projected to the same Carrington grid, the location of each event can be different in the two data sets. Indeed, the separation angle between the two vantage points induces a parallax shift for those events located above or below the projection sphere. The contour of each event detected in HRI_{EUV} was shifted by the amount measured by Zhukov et al. (2021) to obtain the corresponding contour in AIA. In the case of spatially overlapping events, this can cause the classification mask (the union of the contours at each time step) to have a different shape in AIA than in HRI_{EUV}. This is the case for the area shown in Fig. 3 in which two successive events, peaking at 14:54:30 UT and 14:55:04 UT, are overlapping and do not have the same height, and thus not the same parallax shift.

We estimate the background emission at each pixel using the `open-cv` implementation of the inpainting method of Bertalmio et al. (2001). This method estimates the intensity inside the mask, by matching the intensity and intensity gradients at its boundary. This operation is performed at each time step. Whenever this background subtraction is applied to the analysis, it will be mentioned explicitly in the text.

Figure 3 (b) shows an example of the result from this treatment. We have selected a pixel inside the mask (pixel 1 in Fig. 3 (a)) and we plotted the light curves as measured in the HRI_{EUV} and AIA channels (dots), together with their calculated background emission (solid lines). For display purposes, original and background subtracted light-curves are normalized to the standard deviation of the original. To plot all the curves on the same panel, we separated vertically the curves from a given channel by an arbitrary value of 5. The error bars are the root mean square of the photon shot noise (as computed in Appendix A) and read noise components. Boerner et al. (2012) provides the read noise for all the AIA bands. For HRI_{EUV}, it is estimated to be 1.5 DN. In this figure, the light curves of all channels but AIA 94 and 335 have a similar behavior. In the AIA 94 and 335 channels, the event in pixel 1 is not detected above the noise. The absence of signal in these two bands is caused by their low response (see Fig. 2) and is common for most of the events.

Figure 3 (c) shows, for a comparison, the same as Fig. 3 (b) for a representative QS pixel (pixel 2 in Fig. 3 (a)). We see apparently uncorrelated fluctuations of the intensity.

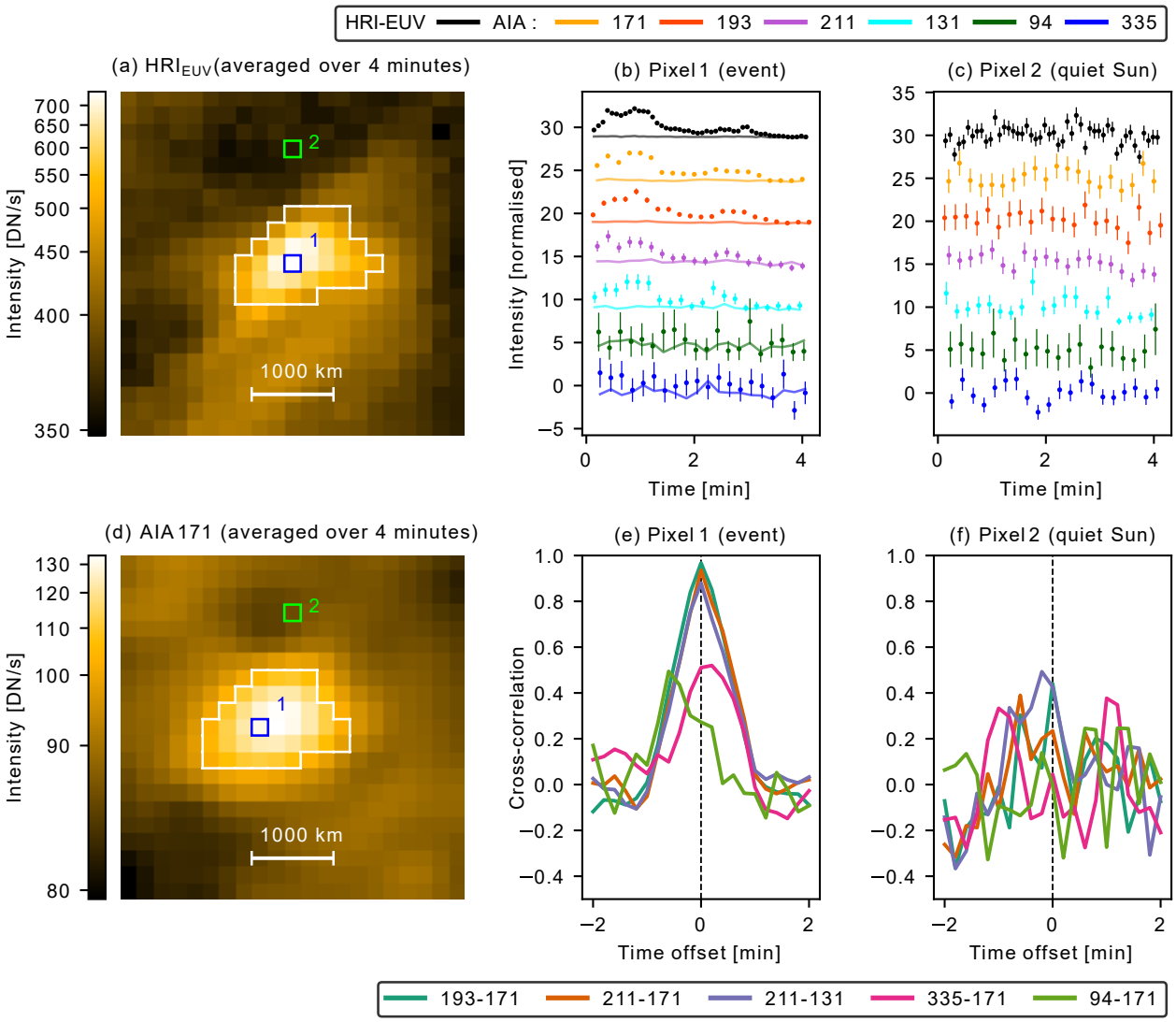

Fig. 3. Images of HRI$_{EUV}$ (a) (14:54:00 UT to 14:58:05 UT) and AIA 171 Å (d) (14:57:45 UT to 15:01:57 UT) averaged in time over their respective sequence on 2020 May 30. Both images are centered around Carrington coordinates (275.00, 9.07)°. The white contours represent the masks that isolate the event pixels from the QS ones. Pixels 1 and 2 are selected, respectively, as example for event pixel and QS pixel. (b) Light curves in pixel 1 for HRI$_{EUV}$ and the AIA channels original data (dots) and background data estimated with "inpainting" algorithm (solid curves). For each channel, both curves are normalized over the standard deviation over time of the original data (dots). (c) light curves in pixel 2 for the same channels of (b), normalized to their standard deviation over time. Different couples are separated by an arbitrary value of 5. The error bars in sub-figures (b) and (c) are computed from the shot and read noises. (e) and (f) show the cross-correlation as a function of the time offset between the AIA light curves for, respectively, pixels 1 (b) and 2 (c).

3.2. Time lags

In the following, we describe the computation of time lags between couples of AIA light curves. The time lags are defined as the temporal offset between the two light curves that yields the maximum Pearson's cross-correlation coefficient.

By design, the six channels' images are not co-temporal. For this reason, we resample the light curves on the timeline of the 171 band using linear interpolation before applying the cross-correlation procedure. The latter is performed on a range of temporal offsets of ±2 minutes, with 12 s steps. A finer estimate of the time lag is obtained by parabolic interpolation around the maximum.

Figures 3 (e) and (f) show the results of this analysis for the AIA pixels 1 and 2. We plot the values of the correlation as a function of the time offset in time applied between the two light curves. For the event pixel, we chose three couples with the high SNR (193 – 171, 211 – 171, 211 – 131). They have a strong correlation peak at near-zero offsets: 0.3 s for 193-171, 0.8 s for 211 – 171, and −0.6 s for 211 – 131.

The other two curves (335 – 171 and 94 – 171) involve low SNR bands, and have a maximum of correlation at a time offset different from 0. They are positive for 335 – 171 (7.8 s) and negative for 94 – 171 (−3.2 s), with a maximum correlation below 0.5. The SNR is low in the 335 and 94 bands and the peak correlation is of the order of that found in the QS (Fig. 3 (f)). We will discuss the significance the cross-correlations involving low SNR bands in Sect. 4.1 and 4.2. Figure 3 (f) shows the results for the selected QS pixel: clearly there is no strong correlation at any time offset and for any pair of AIA channels.

Figure 4 displays the maps of AIA intensity averaged over the sequence (upper row), time lag (middle row) and maximum

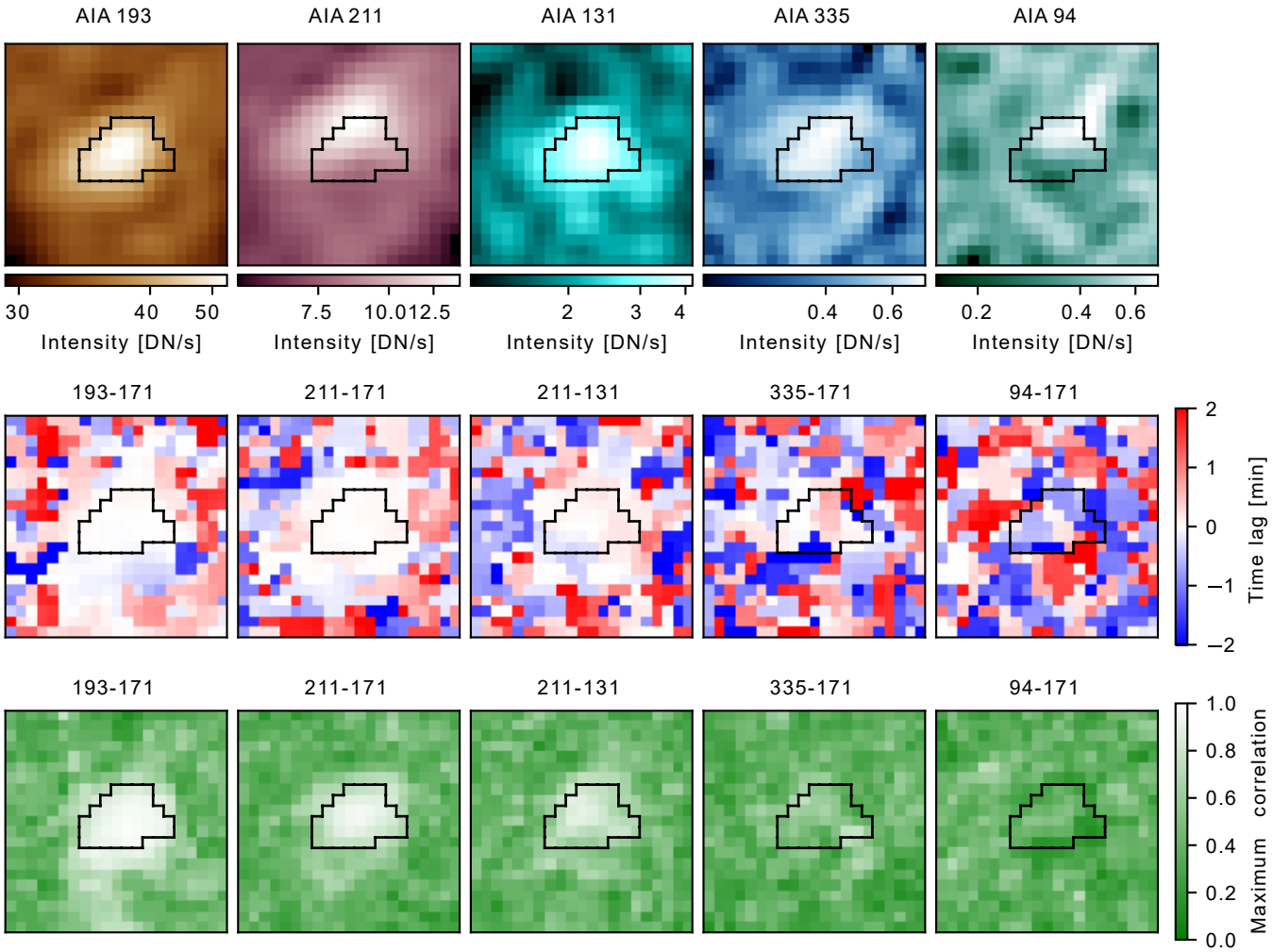

Fig. 4. Top row: intensity maps for five AIA bands (averaged over the temporal sequence) showing the event of Fig. 3 (a) and (d). The "event" region is identified by the black contour. Middle and bottom rows: time lag and associated maximum correlation maps for five couples of AIA bands. These are the result of the pixel-by-pixel cross-correlation analysis. The maximum correlations of the events decreases as the intensities of the involved AIA channels decrease.

of cross-correlation (lower row) for the area shown in Fig. 3. We notice that the emission is not co-spatial in all bands: The intensity maps show a displacement of emission peak for AIA 211 and 94 (even though the signal is very low for AIA 94). Since the AIA channels are all co-aligned, this could be due to the thermal structure of the observed features. These observations show the importance of analyzing the plasma evolution pixel by pixel, as opposed to averaging the intensity over the event surface. While doing the latter might increase the SNR, it will mix light curves of regions at different temperatures.

The bands in the top row of Fig. 4 are ordered by decreasing mean intensity and thus decreasing SNR. In the bottom row, within the mask we see correspondingly decreasing correlation values. Higher correlation values are associated with spatially coherent near-zero time lags, whereas lower correlations show an apparently random distribution of the time lags.

4. Results

In Sect. 4.1 we present the statistical analysis over the whole field of view of the data. Section 4.2 discusses the effect of the SNR on the results. Section 4.3 estimates the effect of the background on the time lag analysis.

4.1. Zero time lags

For the event pixels, Fig. 5 displays the time lag and the maximum correlation 2D histograms. We choose nine representative AIA couples, covering a wide range of temperature sensitivities. Here, the estimated background has been subtracted from the event pixel intensity.

The green dashed lines are the 80, 90, and 95% confidence levels, as computed in Appendix A. The counts above the 95 % level are at most 5 % likely to occur by chance. For most of the couples, a significant number of pixels is centered about short time lags (below the twelve seconds cadence), and are above the 95 % confidence level in cross-correlation. This part of the distribution is therefore statistically significant. On the contrary, 94 – 335 shows no significant pixel counts above the 95 % confidence level, which matches the contour of the 2D histogram. Given that these bands are largely affected by noise, this vali-

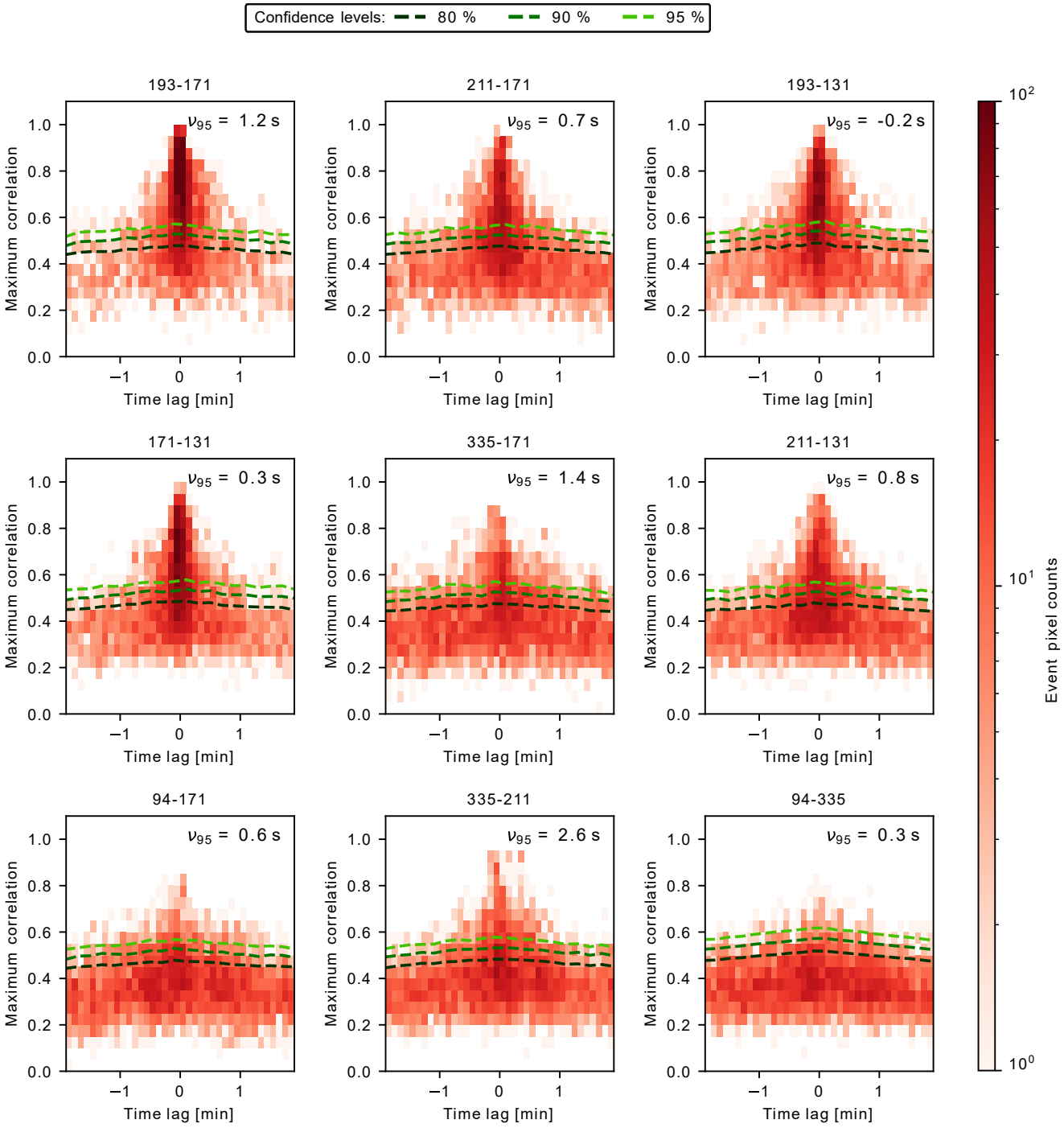

Fig. 5. 2D histograms (shades of red) of time lags and maximum correlations for nine couples of AIA channels, for the 4451 event pixels of the $\mathrm{HRI_{EUV}}$ field of view. The estimated background has been subtracted. The green dashed lines are the confidence levels, derived in Appendix A. The ν_{95} parameter quantifies the asymmetry of the time lag distributions. It is the average of the event time lags above the 95 % confidence level, weighted by their respective maximum correlations.

dates *a posteriori* the principle of computing confidence levels from uncorrelated light-curves (Appendix A).

While the time lags are near zero, the distributions are slightly asymmetric. This can be quantified by the parameter ν_{95}, which represents the average of the time lag values above the 95 % confidence level, weighted by their maximum correlation. Apart from the 335 – 211 couple, all the asymmetries are below the exposure time of 2 s. For 335 – 211, the positive asymmetry is above the exposure time but below the temporal resolution.

4.2. Influence of the signal level

The main panels of Fig. 6 display the 2D histograms of the average intensity over the time sequence versus the maximum correlations for the two AIA couples: 193 – 171 (left column, high

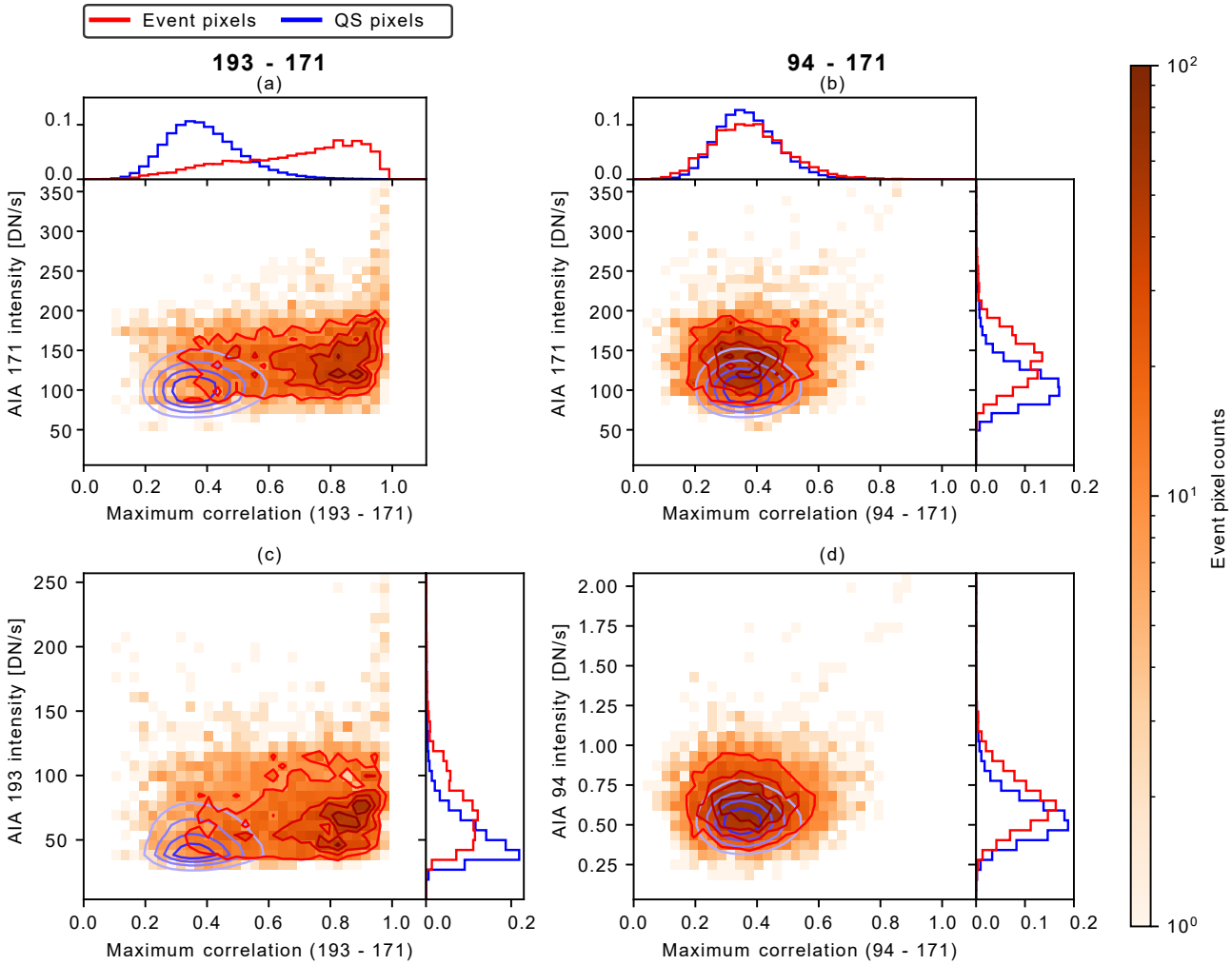

Fig. 6. Main panels: histograms of the time-averaged intensity, as a function of the maximum cross-correlation, in the whole HRI_{EUV} field of view. The left and right columns show the results for, respectively, the 193-171 and the 94-171 couples. The 2D orange histograms are the counts of event pixels. The 2D red and blue contours correspond to the [20, 40, 60, 80] percentiles of the events and the QS pixels distributions, respectively. The margin histograms are normalised by their total number of counts. The right margin histogram of (a) is not displayed, as it is a repetition of the one of (b). Similarly, top margin histograms of (c) and (d) are respectively the ones of (a) and (b).

– high SNR) and 94 – 171 (right column, low – high SNR). The bottom (respectively top) row displays the intensity of the first (respectively second) band of the pair. The orange distributions and red contours refer to the event pixels, and the blue contours to the QS pixels. For the 193 – 171 couple (Fig. 6 (a) and (c)), the event pixels distribution shows a wide range of possible correlation values, as opposed to the QS pixels one. The latter is more compact, and centered around lower maximum correlation and intensity values. On the contrary, the 171 – 94 case shows both events and QS pixels histograms sharing a similar compact shape. This is mostly due to the lower intensity, and thus lower SNR, in the 94 band.

The intensity distributions, which are displayed in the right margin histograms of Fig. 6, peak at higher values for the event pixels than for the QS, for every channel. This implies that, on average, the HRI_{EUV} events are also visible in the AIA channels. The most significant difference between the two AIA couples shown in the figure is their maximum correlation distributions, displayed in the top margin histograms. Indeed, while the event pixels distribution peaks at higher correlation values than the QS ones for 193 – 171, both distributions share a similar shape for 94 – 171.

As shown in the intensity distributions of the right margin histograms, the signal in 94 band is much lower than in the other two bands. Given an exposure time of 3s, the 94 band intensity distributions (Fig. 6 (d)) are close to the read noise value of 1.14 DN. The SNR of the median intensity over the QS in the field of view is 13.7, 9.5 and 0.7 for the 171, 193 and 94 bands respectively. Thus in the 94 band, the noise dominates and the events, if present in the band, remain undetected for most of the cases (see Fig. 3, b as an example). This is why, in the 94 – 171 case, the maximum correlation distributions of the events and the QS pixels share the same statistical behavior: most of the signal in this band originates from the noise. In Fig. 5, it explains the low number of significant time lags for the couples 94 – 171 and 94 – 335.

4.3. Influence of the background subtraction

According to Fig. 6, the AIA 171 intensities distribution of the events peaks only about 1.3 times higher values than the QS ones. Therefore, the background largely contributes to the overall signal. This is why it is necessary to evaluate its influence on the cross-correlations, which we illustrate using the couple 193–171. Figure 7 displays the time lag and the maximum correlation distributions without (left) and with (right) the subtraction of the estimated background component (as described in Sect. 3.1). The 2D histogram of event pixels is represented in shades of red, while the distribution of QS pixels is visualized by blue contours. In the margins, the 1D event pixels distributions are displayed in red and the QS ones in blue. The green histograms correspond to the uncorrelated light curves used to compute the confidence levels (Appendix A).

As in Fig. 5, the events distributions peak at high correlation values, and are concentrated around short time lags. The impact of the background intensity on the events distributions is visible when comparing Fig. 7 (a) with (b): the time-lags and their asymmetries are mostly unchanged.

However, when removing the background, the distribution of the event pixels is flattened (most visible in the margin histogram) and the counts are redistributed in the low correlation, random time lag wings. This has two causes. First, the noise from the QS is propagated to the background by the inpainting (Sect. 3.1), and in turn to the background-subtracted light curves. Thus, the correlations are lowered in this case. Second, the QS signal is partly correlated around zero time lag. This forms the high-correlation tail visible in the blue contours of Fig. 7 (a). Subtracting the background removes this correlated signal, which also lowers the correlations. To conclude, removing the background isolates the contribution of the events to the time lags. Thus, the time lags in Figures 7 (b) and 5 are a property of the events and not of the QS.

5. Discussion

In this work, we have presented the results from the statistical analysis of the time lags measured in the AIA data for the small scales EUV brightening (the "campfires") cataloged by Berghmans et al. (2021). This catalog has the unique property of collecting the tiniest and most rapid brightening ever observed, which are the manifestation of physical processes probably already known, but now observed over shorter temporal and spatial scales. For this reason, we preferred to use the general name of "EUV events".

Our observational work points to the following result: the events are characterized by short time lags (within ±12 s) and high correlations. We verified that these results are statistically significant, and are not caused by background variations alone. In comparison, the QS mostly exhibits random time lags with lower correlations. It is possible that the timescales of thermal changes between events and the surrounding areas are different, the latter being much longer than the maximum time lags considered here.

To our knowledge, this is the first time that the time lags associated with small scale EUV brightenings and their surroundings have been statistically characterized. Earlier works, as mentioned in the introduction, and which used this technique, reported zero time lags in the QS surrounding active region loops, without taking into account the possible presence of small scale brightenings.

Concerning the interpretation of the short time lags, there are three possible scenarios that can be raised, and which we are going to discuss in the following:

1. The observed events do not reach the peak temperatures of the response function (∼ one million degree);
2. The observed events reach coronal temperatures (> 1 MK) but their fast cooling, their sub-pixel multithermal structure, and the width of the AIA response function, prevent us from detecting significant time lags;
3. The observed events are the transition region (∼ 1MK) emission of long and hot (i.e ∼ 10 – 100 Mm, ∼ 3 MK ; Reale 2014) loops, which are heated impulsively.

Let us start with the interpretation given by the scenario 1. Looking at the most intense bands of AIA (Figure 2), we understand that a time lag zero arises when the plasma temperature does not reach the peak of the 171 band. At the temperatures below this peak, all the bands behave similarly, and so do the light curves.

Furthermore, the observational properties (low-lying, short time lags) of these events resemble what is observed by Winebarger et al. (2013) for the "Hi-C loops" ($T_e \sim 10^5$ K and $n_e \sim 10^{10}$ cm^{-3}) in the inter moss loops areas. Their time lag analysis on the AIA light curves also displayed near-zero time lags, which brought them to conclude that the loops did not reach one million degree. Their interpretation was the observation of impulsively, low-energy (nanoflares) heated loops which cool rapidly due to their small length. Given the similarities of the HRI brightenings to these events, we suggest that they may have a similar physical origin, being the result of an impulsive heating.

For such cold events to be visible in the AIA bands and in $\mathrm{HRI_{EUV}}$, they should be quite dense. We did a first order estimation of their density, using an average value of the background-subtracted event intensity on AIA 171 and assuming an isothermal plasma. We obtained $n_e \sim 10^9$ cm^{-3} for $T_e = 1.3 \times 10^6$ K and $n_e \sim 10^{10}$ cm^{-3} for $T_e = 3 \times 10^5$ K. The latter supports the result of Winebarger et al. (2013).

However, we must consider possible differences between the Hi-C loops and our $\mathrm{HRI_{EUV}}$ events. First, as mentioned, the observed solar region is not the same. But small low-lying cool loops ($T_e \leq 0.5$ MK) are observed in the QS (Hansteen et al. 2014), and are ubiquitous along the supergranular cell boundaries in the solar upper atmosphere (see for instance, Feldman et al. 1999; Sánchez Almeida et al. 2007, and references therein). And since there is no distinction between supergranular cells in QS and AR, we expect to observe similar events in both regions. Berghmans et al. (2021) showed with $\mathrm{HRI_{Ly\alpha}}$ observations that the $\mathrm{HRI_{EUV}}$ events are organised mostly around the supergranular network.

Another difference between the Hi-C and the $\mathrm{HRI_{EUV}}$ events are their estimated temperature, around $T_e \approx 0.25 \pm 0.06$ MK for the first case (Winebarger et al. 2013) and around 1.3 ± 0.1 MK for the latter case (Berghmans et al. 2021). Again, if we are looking at similar events in the two cases, we suggest that such discrepancy may be due to the uncertainties in the data, the inversion methods and associated assumptions applied to relatively broad band instruments, as for these imagers. Indeed, the measurement of the temperature of these events is very challenging. For instance, Schonfeld & Klimchuk (2020) showed that often the cool plasma emission dominates the bands, even though the hot plasma is there.

Let us now assume that we are in the scenario 2. A time lag close to zero for AIA bands has been predicted in the TR emission of active region coronal loops heated by nanoflares (Viall & Klimchuk 2015, see also references therein). They showed

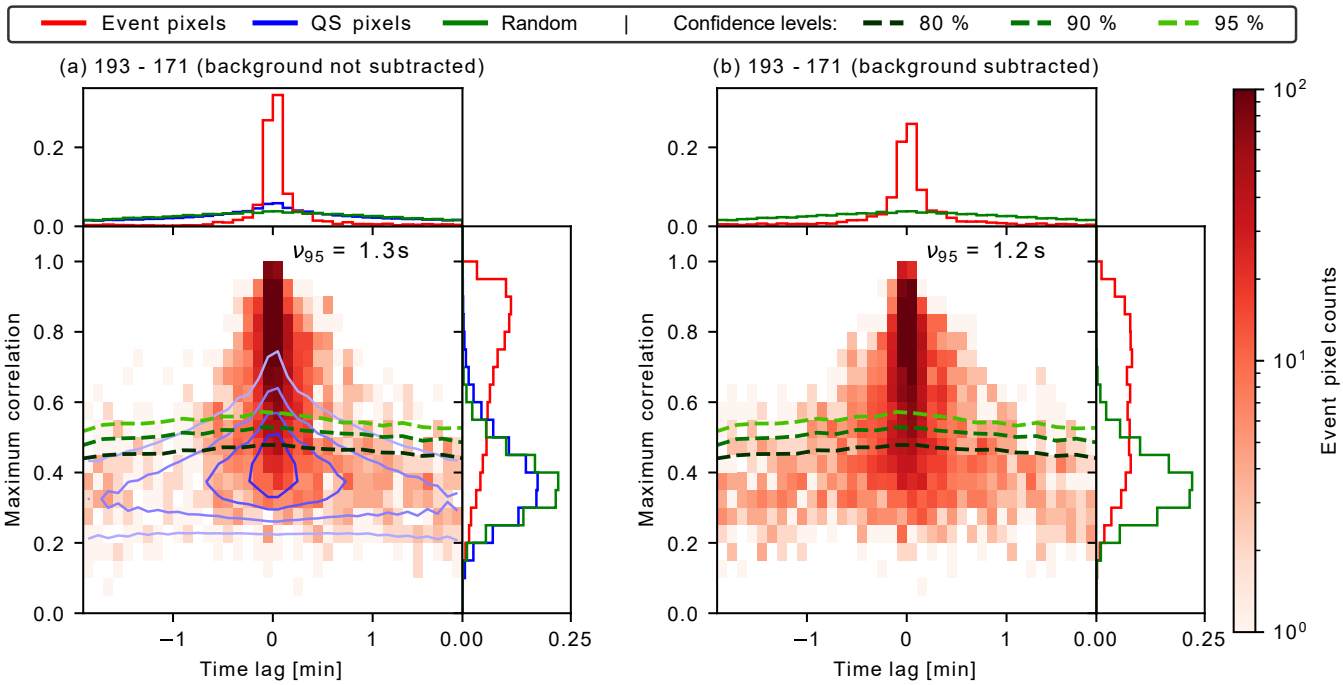

Fig. 7. Margin and 2D histograms of time lags and associated maximum correlation values for the couple 193-171. Sub-figure (a) in red shows the original distribution for the event pixels, sub-figure (b) shows the background subtracted event pixels. The blue contours in the central panel of sub-figure (a) are the [20, 40, 60, 80] % percentiles of the QS pixels distribution. The green colors in the main panels are the confidence levels, and the distributions of the light curves used to compute them is plotted with the same color in the margin histograms. The margin histograms are normalised by their total number of pixels. The parameter $\nu_{>95}$ is defined as in Fig. 5.

that the combination of the multi-temperature sensitivity of the AIA bands, combined with the almost constant pressure property of the TR and its variable extension along the loop during the heating-cooling phases, result in a narrower time lag with respect to the coronal emission part of the loop. To be emphasized here that the TR of a loop is defined as the region where the thermal conduction acts as a plasma coolant, contrary to the coronal region where it acts as a heater (e.g. Klimchuk et al. 2008). While the presence in the simulation of short time lags for all the AIA couples corroborates our results, the loops modeled by Viall & Klimchuk (2015) are much longer than what we are dealing with here ($L \approx 30 - 50$ Mm, with respect to $0.4 - 4$ Mm). Moreover, in those simulations, a clear different signature in the time lag exists between TR and coronal emission, while this is not visible in our data. This could be possibly explained by the short cooling time from coronal temperatures of one of these tiny loops. For instance, for the shorter loops (~ 0.4 Mm) detected by $\mathrm{HRI_{EUV}}$ at a temperature of ~ 1.3 MK and density of $n_e = 10^{10}\mathrm{cm}^{-3}$ the cooling time is about 14s.
It is possible that our time lag method is not sensitive enough, due to the AIA cadence of 12 s, to detect both TR and coronal emission populations of short time lags. We propose to investigate further this aspect in the future through numerical simulations. The small asymmetries we have in our time lag distributions are below the cadence of our observation. We would need a higher temporal resolution data to corroborate such result. The cadence should be at last similar to the one of $\mathrm{HRI_{EUV}}$, where the emission variation of the event is better captured. At present, we verified that the measured time lags are independent of the event's duration.

Concerning the scenario 3, if such large loops exist in the QS, they remain undetected by the AIA channels, meaning that they would have a very low density. Without independent evidence that this is the case, we exclude for now this possibility.

In conclusion, in the picture of impulsive heating phenomena acting in the QS region, and considering the wide temperature response of the AIA bands, our results appear also to be consistent with predominantly fast cooling plasma from more than 1 MK, that is satisfying our scenario 2. Consistently with this picture are the results from a 3D MHD simulations using MURaM code by Chen et al. (2021). Here magnetic reconnections in the coronal part of small QS loops produced events with properties similar to what observed in $\mathrm{HRI_{EUV}}$. They noticed that the simulated $\mathrm{HRI_{EUV}}$ emission only showed the apex of the heated loop, where the lower density allows the available stored energy to heat the plasma up to $\approx$ 1.3 MK, even though some hotter temperatures could also be reached.

To summarize, our results are consistent with two possible scenarios: either the events do not reach coronal temperatures, or they do, but they cool faster than the AIA temporal resolution. It is possible that the two scenarios coexist, as the $\mathrm{HRI_{EUV}}$ catalog does not separate events produced by different physical processes. The AIA cadence and the multithermal nature of the bands do not allow separating the emissions from the possible cool and hot plasma along the line of sight.

To solve the ambiguity on the temperature, we need to use spectroscopic data. This has been done recently by using the Spectral Imaging of the Coronal Environement (SPICE) instrument on board Solar Orbiter (Huang et al. submitted to this issue). They investigated a few HRIEUV events and came to the conclusion that the studied events do not show significant emission at temperatures higher than that of Ne VIII (0.63 MK).

Although such spectroscopic analysis needs to be extended to a larger sample to better quantify the fraction of events not

reaching high temperatures, we find it to support our conclusion that quiet Sun small-scale EUI brightenings are in most cases largely dominated by cool emission.

Further investigations are needed to confirm this idea. For these reasons, we plan to extend our methodology to forward modeling constrained by spectroscopic data.

Acknowledgements. The authors gratefully thank J.A. Klimchuk for the fruitful discussions and suggestions. A.D. acknowledges the funding by CNES and EDOM. S.P. acknowledges the funding by CNES through the MEDOC data and operations center. G.P. was supported by a CNES postdoctoral allocation. P.A. and D.M.L. are grateful to the Science Technology and Facilities Council for the award of Ernest Rutherford Fellowships (ST/R004285/2 and ST/R003246/1, respectively). The ROB team thanks the Belgian Federal Science Policy Office (BELSPO) for the provision of financial support in the framework of the PRODEX Programme of the European Space Agency (ESA) under contract numbers 4000134474 and 4000136424. This paper uses the Solar Orbiter/EUI data release 1.0 https://doi.org/10.24414/WVJ6-NM32. Solar Orbiter is a space mission of international collaboration between ESA and NASA, operated by ESA. The EUI instrument was built by CSL, IAS, MPS, MSSL/UCL, PMOD/WRC, ROB, LCF/IO with funding from the Belgian Federal Science Policy Office (BELSPO/PRODEX PEA 4000134088, 4000112292, 4000117262, and 400013447); the Centre National d'Etudes Spatiales (CNES); the UK Space Agency (UKSA); the Bundesministerium für Wirtschaft und Energie (BMWi) through the Deutsches Zentrum für Luft- und Raumfahrt (DLR); and the Swiss Space Office (SSO). This work used data provided by the MEDOC data and operations centre (CNES / CNRS / Univ. Paris-Saclay), http://medoc.ias.u-psud.fr/. This research used version 0.6.4 (Barnes et al. 2021) of the `aiapy` open source software package (Barnes et al. 2020).

References

Antolin, P., Pagano, P., Testa, P., Petralia, A., & Reale, F. 2021, Nature Astronomy, 5, 54
Aschwanden, M. J. & Parnell, C. E. 2002, ApJ, 572, 1048
Auchère, F., Andretta, V., Antonucci, E., et al. 2020, A&A, 642, A6
Auchère, F., Bocchialini, K., Solomon, J., & Tison, E. 2014, A&A, 563, A8
Barnes, W., Cheung, M., Bobra, M., et al. 2021, aiapy
Barnes, W. T., Cheung, M. C. M., Bobra, M. G., et al. 2020, Journal of Open Source Software, 5, 2801
Berghmans, D., Auchère, F., Long, D. M., et al. 2021, A&A, 656, L4
Berghmans, D., Clette, F., & Moses, D. 1998, A&A, 336, 1039
Bertalmio, M., Bertozzi, A., & Sapiro, G. 2001, in Proceedings of the 2001 IEEE Computer Society Conference on Computer Vision and Pattern Recognition. CVPR 2001, Vol. 1, I–I
Boerner, P., Edwards, C., Lemen, J., et al. 2012, Sol. Phys., 275, 41
Buchlin, E. & Velli, M. 2007, ApJ, 662, 701
Chen, Y., Przybylski, D., Peter, H., et al. 2021, A&A, 656, L7
Chitta, L. P., Peter, H., & Young, P. R. 2021, A&A, 647, A159
Crosby, N. B., Aschwanden, M. J., & Dennis, B. R. 1993, Sol. Phys., 143, 275
De Pontieu, B., Title, A. M., Lemen, J. R., et al. 2014, Sol. Phys., 289, 2733
Del Zanna, G., Dere, K. P., Young, P. R., & Landi, E. 2021, ApJ, 909, 38
Dere, K. P., Landi, E., Mason, H. E., Monsignori Fossi, B. C., & Young, P. R. 1997, A&AS, 125, 149
Feldman, U., Widing, K. G., & Warren, H. P. 1999, ApJ, 522, 1133
Froment, C. 2016, Theses, Université Paris Saclay (COmUE)
Froment, C., Antolin, P., Henriques, V. M. J., Kohutova, P., & Rouppe van der Voort, L. H. M. 2020, A&A, 633, A11
Froment, C., Auchère, F., Aulanier, G., et al. 2017, ApJ, 835, 272
Froment, C., Auchère, F., Bocchialini, K., et al. 2015, ApJ, 807, 158
Gupta, G. R. 2014, A&A, 568, A96, publisher: EDP Sciences
Hahn, M. & Savin, D. W. 2014, ApJ, 795, 111
Hannah, I. G., Hudson, H. S., Hurford, G. J., & Lin, R. P. 2010, ApJ, 724, 487
Hannah, I. G. & Kontar, E. P. 2012, A&A, 539, A146
Hansteen, V., De Pontieu, B., Carlsson, M., et al. 2014, Science, 346, 1255757
Harra, L., Gallagher, P., & Phillips, K. 2000, A&A, 362
Huang, Z., Teriaca, L., Aznar Cuadrado, R., et al. submitted to this issue, A&A
Innes, D. E. & Teriaca, L. 2013, Sol. Phys., 282, 453
Ireland, J., McAteer, R. T. J., & Inglis, A. R. 2014, ApJ, 798, 1
Kahil, F., Hirzberger, J., Solanki, S. K., et al. 2022, A&A, 660, A143
Klimchuk, J. A., Patsourakos, S., & Cargill, P. J. 2008, ApJ, 682, 1351
Kobayashi, K., Cirtain, J., Winebarger, A. R., et al. 2014, Sol. Phys., 289, 4393
Lemen, J. R., Title, A. M., Akin, D. J., et al. 2012, Sol. Phys., 275, 17
Max-Moerbeck, W., Richards, J. L., Hovatta, T., et al. 2014, MNRAS, 445, 437
McIntosh, S. W., de Pontieu, B., Carlsson, M., et al. 2011, Nature, 475, 477
Moriyasu, S., Kudoh, T., Yokoyama, T., & Shibata, K. 2004, ApJ, 601, L107
Müller, D., St. Cyr, O. C., Zouganelis, I., et al. 2020, A&A, 642, A1
Panesar, N. K., Tiwari, S. K., Berghmans, D., et al. 2021, ApJ, 921, L20
Parker, E. N. 1988, ApJ, 330, 474
Pesnell, W. D., Thompson, B. J., & Chamberlin, P. C. 2012, Sol. Phys., 275, 3
Peter, H., Tian, H., Curdt, W., et al. 2014, Science, 346, 1255726
Raouafi, N. E. & Stenborg, G. 2014, ApJ, 787, 118
Reale, F. 2014, Living Reviews in Solar Physics, 11, 4
Régnier, S., Alexander, C. E., Walsh, R. W., et al. 2014, ApJ, 784, 134
Rochus, P. et al. 2020, A&A, 642, A8
Sánchez Almeida, J., Teriaca, L., Sütterlin, P., et al. 2007, A&A, 475, 1101
Schonfeld, S. J. & Klimchuk, J. A. 2020, ApJ, 905, 115
Shimizu, T. 1995, PASJ, 47, 251
Sukarmadji, A. R. C., Antolin, P., & McLaughlin, J. A. 2022, ApJ, 934, 190
Threlfall, J., De Moortel, I., & Conlon, T. 2017, Sol. Phys., 292, 165
Timmer, J. & Koenig, M. 1995, A&A, 300, 707
Upendran, V. & Tripathi, D. 2021, ApJ, 916, 59
Upendran, V. & Tripathi, D. 2022, ApJ, 926, 138
Van Doorsselaere, T., Srivastava, A. K., Antolin, P., et al. 2020, Space Sci. Rev., 216, 140
Viall, N. M., De Moortel, I., Downs, C., et al. 2021, in Solar Physics and Solar Wind, ed. N. E. Raouafi & A. Vourlidas, Vol. 1, 35
Viall, N. M. & Klimchuk, J. A. 2011, ApJ, 738, 24
Viall, N. M. & Klimchuk, J. A. 2012, ApJ, 753, 35
Viall, N. M. & Klimchuk, J. A. 2015, ApJ, 799, 58
Viall, N. M. & Klimchuk, J. A. 2017, ApJ, 842, 108, aDS Bibcode: 2017ApJ...842..108V
Wilhelm, K., Curdt, W., Marsch, E., et al. 1995, Sol. Phys., 162, 189
Winebarger, A. R., Cirtain, J., Golub, L., et al. 2014, ApJ, 787, L10
Winebarger, A. R., Walsh, R. W., Moore, R., et al. 2013, ApJ, 771, 21
Young, P. R., Tian, H., Peter, H., et al. 2018, Space Sci. Rev., 214, 120
Zhukov, A. N., Mierla, M., Auchère, F., et al. 2021, A&A, 656, A35
Zouganelis, I., De Groof, A., Walsh, A. P., et al. 2020, A&A, 642, A3

Appendix A: Computation of the confidence levels

The cross-correlation of two uncorrelated random time series has a nonzero probability of resulting in a time lag with a nonzero value for the maximum correlation. This is why the interpretation of our time lag results is challenging, especially for couples involving low to medium SNR AIA channels, such as 131, 94 and 335 which are noise dominated in several pixels.

For our goal we adopted a Monte-Carlo approach inspired by Max-Moerbeck et al. (2014). We computed the time lags (corresponding to the maximum cross correlation) between many uncorrelated simulated AIA light curves to estimate the probability of chance occurrence of each time lag value.

The simulated light curves are built using the observational results that the coronal emission has a temporal Power Spectral Density (PSD) that can be modeled by a power law (Auchère et al. 2014; Gupta 2014; Threlfall et al. 2017). Specifically, for the QS, Ireland et al. (2014) fitted the exponents $n = 1.72 \pm 0.01$ for AIA 171 and $n = 2.20 \pm 0.01$ for AIA 193. To keep the empirical model simple, we adopted a power law with exponent $n = 2$ for all the AIA channels. From this PSD, we generate 10^5 random light curves of 4 min length and 12 s cadence using the method described in (Timmer & Koenig 1995).

The obtained time series $\hat{I}$(t) (in arbitrary units) are converted into Digital Number (DN) as the follow:

$$I(t)\ [\mathrm{DN}] = \left(\hat{I}(t) - \mu_{\hat{I}}\right) \frac{\sigma_{\mathrm{DN}}}{\sigma_{\hat{I}}} + \mu_{\mathrm{DN}} \tag{A.1}$$

where $\mu_{\hat{I}}$ and $\sigma_{\hat{I}}$ are, respectively, the mean and standard deviation of $\hat{I}$(t); μ_{DN} and σ_{DN} are the spatial mean intensity and the standard deviation derived from the first image of the AIA sequence (see Fig. 1 (d)).

Photon noise is then added by picking random values from a Poisson distribution peaking at the average photons per image. We assume it to be equal to the incident photons I(t). Negative intensity values are set to zero. Next, we simulate the regular AIA acquisition chain by re-converting the time series into DN. Read noise is then added, in the form of a normal distribution of mean zero and standard deviation σ_{RN}. Using the inverse of the camera gain, $I(t)$ is converted into photons. All the conversion constants are taken from the initial AIA calibration (Boerner et al. 2012).

The resulting time series are now used for the time lag analysis applied to each of the AIA couples used in Sect. 4.1 and 4.3.

The time lags and maximum correlation distributions of these random light curves are displayed for the couple 193-171 in the margin histograms of Fig. 7. The confidence levels are defined as the [80 %, 90 %, 95 %] percentiles of the maximum correlation distribution. They are displayed as green dashed lines in Fig. 7 and Fig. 5. According to our simulation, counts above the 95 % confidence level are at most 5 % likely to be caused by chance.

Appendix B: Event-based time lag analysis

The main work we have presented is based on the single pixel analysis. Here we summarize the results from the full-event investigation in order to verify if the resulting thermal behavior reflects the one deduced with the single-pixel analysis.

Both the pixel-based and the full-event approaches have their advantages. The full-event approach increases the SNR of the light curves, as it is represented by the averaged intensity over the selected event area, but does not separate the "cold" and the "hot" pixels populations. This is because inside an "event surface", one pixel might reach a higher temperature compared with the others. The high temperature pixel and the lower temperature ones appear as separate counts in the resulting figures of the pixel-based approach (Fig. 5). On the contrary, the temperature associated with the average intensity will be something in between the hottest and cooler pixels, so reducing the temperature excursion over time. Each event area is a single count in the statistical analysis (Fig. B.1).

To build the single-event light curves, we proceeded by spatially averaging the light curves within each event mask. The time lag analysis is then applied to these new time sequences in the same way as it was done for the pixel-based approach (Sect. 3.2).

The results of the analysis are displayed in Fig. B.1. The time lags are centered around short values (>12s), above the 95 % confidence levels. There is no noticeable difference with the pixel-based approach (Fig. 5), apart from small variations in the asymmetries ν_{95}, which remains close to the exposure time. The variations are probably caused by the lower number of counts above the 95 % confidence level, compared with the pixel-based approach. It decreases the statistical significance of the asymmetry, and the events should be studied individually.

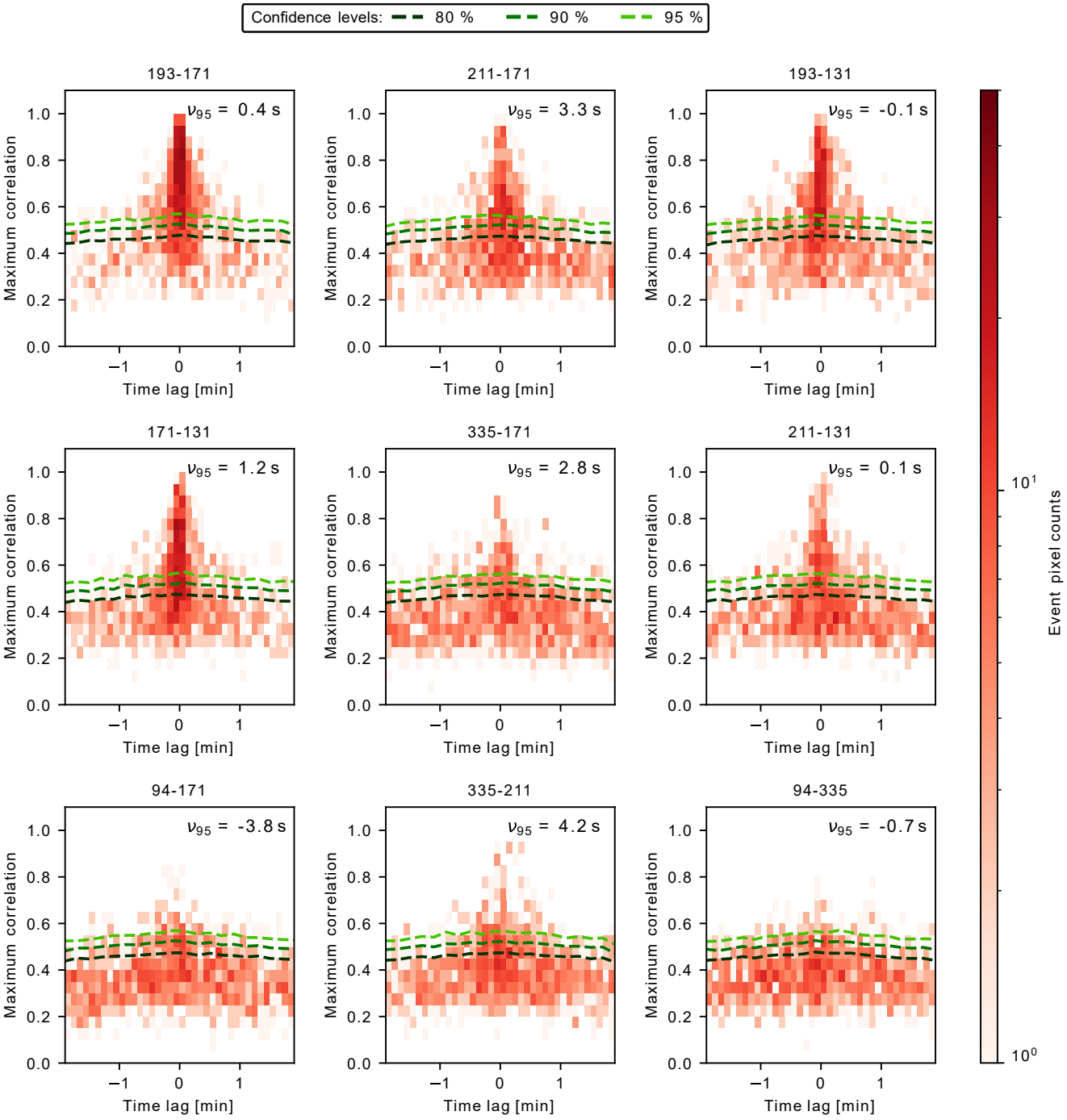

Fig. B.1. Same as Fig. 5, but with a full-event approach, as opposed to a pixel-based one. For every 1314 events, the light curves are spatially averaged over each of their respective event surface. Then, time lag extraction is performed similarly as the pixel-based approach (Sect. 3.2). The estimated background has been previously subtracted on event pixels with the "inpainting" algorithm.